



HAL
open science

Experimental Wind Characterization with the SuperCam Microphone under a Simulated martian Atmosphere

Baptiste Chide, Naomi Murdoch, Yannick Bury, Sylvestre Maurice, Xavier Jacob, Jonathan P. Merrison, Jens J. Iversen, Pierre-Yves Meslin, Marti Bassas-Portús, Alexandre Cadu, et al.

► **To cite this version:**

Baptiste Chide, Naomi Murdoch, Yannick Bury, Sylvestre Maurice, Xavier Jacob, et al.. Experimental Wind Characterization with the SuperCam Microphone under a Simulated martian Atmosphere. *Icarus*, 2021, 354, pp.114060-114072. 10.1016/j.icarus.2020.114060 . hal-03039928

HAL Id: hal-03039928

<https://hal.science/hal-03039928>

Submitted on 4 Dec 2020

HAL is a multi-disciplinary open access archive for the deposit and dissemination of scientific research documents, whether they are published or not. The documents may come from teaching and research institutions in France or abroad, or from public or private research centers.

L'archive ouverte pluridisciplinaire **HAL**, est destinée au dépôt et à la diffusion de documents scientifiques de niveau recherche, publiés ou non, émanant des établissements d'enseignement et de recherche français ou étrangers, des laboratoires publics ou privés.



Open Archive Toulouse Archive Ouverte (OATAO)

OATAO is an open access repository that collects the work of some Toulouse researchers and makes it freely available over the web where possible.

This is an author's version published in: <https://oatao.univ-toulouse.fr/26971>

Official URL : <https://doi.org/10.1016/j.icarus.2020.114060>

To cite this version :

Chide, Baptiste and Murdoch, Naomi and Bury, Yannick,... [et al.] Experimental Wind Characterization with the SuperCam Microphone under a Simulated martian Atmosphere. (2021) Icarus, 354. 114060-114072. ISSN 00191035

Any correspondence concerning this service should be sent to the repository administrator:

tech-oatao@listes-diff.inp-toulouse.fr

Experimental Wind Characterization with the SuperCam Microphone under a Simulated Martian Atmosphere

Baptiste Chide^{a,b}, Naomi Murdoch^a, Yannick Bury^a, Sylvestre Maurice^b, Xavier Jacob^c,
Jonathan P. Merrison^d, Jens J. Iversen^d, Pierre-Yves Meslin^b, Marti Bassas-Portús^a,
Alexandre Cadu^a, Anthony Sournac^a, Bruno Dubois^e, Ralph D. Lorenz^f, David Mimoun^a,
Roger C. Wiens^g

^a*Institut Supérieur de l'Aéronautique et de l'Espace (ISAE-SUPAERO), Université de Toulouse, 31400
Toulouse, France*

^b*IRAP-CNRS, Université Toulouse III, 31400 Toulouse, France*

^c*IMFT-CNRS, Université Toulouse III, 31400 Toulouse, France*

^d*Department of Physics and Astronomy, University of Aarhus, Aarhus, Denmark*

^e*Observatoire Midi-Pyrénées (OMP), Université de Toulouse, Toulouse, France*

^f*Johns Hopkins Applied Physics Laboratory, Laurel, MD 20723, USA*

^g*Los Alamos National Laboratory, Los Alamos, NM 87545, USA*

Abstract

Located on top of the mast of the Mars 2020 *Perseverance* rover, the SuperCam instrument suite includes a microphone to record audible sounds from 100 Hz to 10 kHz on the surface of Mars. It will support SuperCam's Laser-Induced Breakdown Spectroscopy investigation by recording laser-induced shock-waves but it will also record aeroacoustic noise generated by wind flowing past the microphone. This experimental study was conducted in the Aarhus planetary wind-tunnel under low CO₂ pressure with wind generated at several velocities. It focused on understanding the wind-induced acoustic signal measured by microphones instrumented in a real scale model of the rover mast as a function of the wind speed and wind orientation. Acoustic spectra recorded under a wind flow show that the low-frequency range of the microphone signal is mainly influenced by the wind velocity. In contrast, the higher frequency range is seen to depend on the wind direction relative to the microphone. On the one hand, for the wind conditions tested inside the tunnel, it is shown that the Root Mean Square of the pressure, computed over the 100 Hz to 500 Hz frequency range, is proportional to the dynamic pressure. Therefore, the SuperCam microphone will be able to estimate the wind speed, considering an *in situ* cross-calibration with the Mars Environmental Dynamic Analyzer. On the other hand, for a given wind speed, it is observed that the root mean square

32 of the pressure, computed over the 500 Hz to 2000 Hz frequency range, is at its minimum
33 when the microphone is facing the wind whereas it is at its maximum when the microphone
34 is pointing downwind. Hence, a full 360° rotation of the mast in azimuth in parallel with
35 sound recording can be used to retrieve the wind direction.

We demonstrate that the SuperCam Microphone has *a priori* the potential to determine both the wind speed and the direction on Mars, thus contributing to atmospheric science investigations.

36 *Keywords:* Mars 2020 Perseverance rover, SuperCam Instrument, Mars Microphone,
37 Atmosphere, Wind speed, Wind orientation

38 1. Introduction

39 The lower layers of the Mars atmosphere, the planetary boundary layer, that extends
40 from the surface to the free atmosphere, mediates exchanges of heat, volatiles and dust via
41 complex and highly variable wind fields interacting with the ground (see [Read et al. \(2016\)](#)
42 for a detailed review). This highly dynamical layer follows an important diurnal cycle: during
43 the daytime, the low heat capacity of the Martian soil induces a rapid heating, yielding
44 thermal instabilities ([Smith et al., 2004](#)) and vertical convective winds ([Spiga et al., 2010](#)).
45 When solar insolation is at its maximum, stronger convective vortices, called dust-devils,
46 become active, lifting dust at high rotating wind speed, at several tens of meters per second
47 ([Balme and Greeley, 2006](#)). At night, the planetary boundary layer reduces to a stable and
48 stratified layer where surface wind velocity is at its minimum ([Read et al., 2016](#)). Additionally,
49 this lower part of the Martian atmosphere sustains a strong influence of local and regional
50 topography: in terrains with a topography gradient, the nocturnal near-surface air cools,
51 causing downslope katabatic winds whereas the opposite upslope wind takes place in the
52 afternoon ([Spiga, 2011](#)).

53 The behavior of the Martian winds near the surface has been supported by several *in*
54 *situ* measurements from landed missions including Vikings 1 and 2 ([Hess et al., 1977](#)), Mars
55 Pathfinder ([Schofield et al., 1997](#)), Phoenix ([Holstein-Rathlou et al., 2010](#)), Curiosity ([Viúdez-](#)
56 [Moreiras et al., 2019](#)); all landed in the northern hemisphere of the planet. A review of this
57 full data set ([Martínez et al., 2017](#)) points out that wind measurement on Mars has been
58 challenging, due in part to challenges of calibration, and in some cases to hardware failures.
59 Measurements in flat plains exhibit a seasonal variability due to the global circulation with
60 a mean wind speed at its minimum during northern spring and summer ($\sim 3 \text{ m s}^{-1}$ measured
61 by the Viking 2 lander with a maximal peak value up to 8 m s^{-1}) and at its maximum during
62 northern fall and winter (mean value around 5 m s^{-1} but with a maximum that reaches
63 24 m s^{-1} also for the Viking 2 lander). A full 360° progressive rotation of the wind direction
64 over a sol is experienced for flat terrains whereas a sudden diurnal transition from upslope to
65 downslope wind is seen in Curiosity data, due to the close proximity of Mount Sharp. Winds

66 are also seen to respond to weather events such as dust storms with an increase of the wind
67 magnitude during those events.

68 The InSight mission, which landed on November 2018, carries the Auxiliary Payload Sen-
69 sor Suite (APSS) which includes a pair of wind sensor booms that allow monitoring of Martian
70 winds with an unprecedented time coverage ([Banfield et al., 2018](#)). Continuous measure-
71 ments over 220 sols ([Banfield et al., 2020](#)) characterized the diurnal variability with a mean
72 wind speed up to $(10 \pm 4) \text{ m s}^{-1}$ (1σ standard deviation) during the day that can reach a
73 maximal value up to 24 m s^{-1} . At night, during the quieter regime after sunset, it decreases
74 to $(2.0 \pm 0.8) \text{ m s}^{-1}$. Moreover, wind direction reverses from northeast during the day to
75 southeast at night, showing the topographic forcing of the wind. Furthermore, as part of
76 the InSight APSS weather station, a pressure sensor continuously samples the atmosphere
77 with a sampling frequency up to 20 Hz ([Spiga et al., 2018](#)), higher than any other previous
78 instruments. It allows the detection of various atmospheric phenomena ([Banerdt et al., 2020](#);
79 [Murdoch et al., submitted](#)), such as lots of dust-devil-like convective vortices and their as-
80 sociated pressure drops, or infrasounds detected via the seismometer SEIS ([Martire et al., in](#)
81 [press](#)). Daytime turbulence is also studied in this new frequency domain (power spectrum
82 from 50 mHz to 5 Hz), providing new insights into the behavior of mechanisms generating
83 high-frequency pressure fluctuations.

84

85 Scheduled for landing in Jezero crater in February 2021, the Mars2020 Perseverance
86 rover will include the Mars Environmental Dynamic Analyzer (MEDA, [de la Torre Juarez](#)
87 [et al. \(2020\)](#)), a weather station located 1.6 m above the ground, that has heritage from
88 REMS onboard Curiosity and the wind sensors of APSS onboard InSight. It is designed to
89 measure horizontal wind speeds up to 70 m s^{-1} and vertical wind speeds up to 10 m s^{-1} with
90 an accuracy of 1 m s^{-1} over the two axes. The horizontal wind direction is expected to be
91 retrieved with a precision of $\pm 15^\circ$. Integrated on top of the rover mast at a height of 2.1 m,
92 the SuperCam remote-sensing suite ([Wiens et al., 2017](#)) includes a microphone, co-aligned
93 with the telescope line of sight, which will record pressure fluctuations in the 100 Hz to 10 kHz

94 frequency bandwidth. It has been demonstrated that listening to laser-induced sparks from
95 rocks and soils can complement the Laser-Induced Breakdown Spectroscopy investigation
96 ([Chide et al., 2019](#)). Moreover the speed of sound can be deduced from sound wave arrival
97 time and used to evaluate the air temperature and thermal gradient ([Chide et al., 2020](#)). The
98 SuperCam microphone can also monitor sounds generated by the rover, and contribute to
99 basic atmospheric science, thanks to a dedicated standalone mode to record natural sounds
100 for up to 2 min 46 sec at a time, at different pointing directions in azimuth and elevation.
101 Sampling frequency can be set at 25 kHz or 100 kHz.

102

103 Wind-induced pressure fluctuations that pass over microphone membranes result in random-
104 like signal called acoustic noise. Often considered on Earth detrimental to outdoor mea-
105 surements, wind-generated noise has been frequently studied in order to design appropriate
106 windscreens to reduce it ([Strasberg, 1988](#)). In the context of the SuperCam Microphone, the
107 atmospheric and wind-induced noise represents a data set of interest. [Morgan and Raspet](#)
108 ([1992](#)) conducted an experimental comparison between outdoor wind noise with sound pres-
109 sure fluctuations in the 1.6 Hz to 1250 Hz frequency range. Following this study, two sources
110 of wind noise can be distinguished: the pressure fluctuation caused by the intrinsic turbulence
111 of the incoming flow and the noise induced by interaction between the flow, the microphone
112 and its nearby spatial environment. First, the turbulence spectrum of the incoming flow can be
113 separated into frequency ranges that follow the turbulence regimes of the atmosphere ([Walker](#)
114 [and Hedlin, 2009](#); [Murdoch et al., 2016](#)): at very low frequencies, a source region where most
115 of the energy is contained in large scale eddies. Then, the mixing of the atmosphere breaks
116 its large scale eddies into smaller scale eddies without energy loss. This inertial regime at
117 intermediate frequencies can be represented by a power law with an expected spectral slope
118 of $-5/3$ according to the Kolmogorov theory ([Kolmogorov, 1991](#)). At higher frequencies
119 when eddies reach the Kolmogorov scale, friction forces are dominant and their kinetic en-
120 ergy is dissipated into heat. During this dissipation regime, the power spectrum drops very
121 sharply. The noise induced by interaction between the flow and the microphone has a lower

122 level and is expected to depend on the orientation of the microphone relative to the wind
123 flow ([Morgan and Raspet, 1992](#)). [Bass et al. \(1995\)](#) made use of the travel time of turbulent
124 eddies transported into the wind flow to determine the wind speed and orientation using an
125 array of three microphones. In an experimental campaign conducted in the same facility as
126 this study, [Lorenz et al. \(2017\)](#) performed the first qualitative approach of the correlation
127 between the microphone noise spectrum and wind speed under controlled Martian conditions.

128
129 Vortices or turbulent structures generated in the wake and around the SuperCam in-
130 strument can impact acoustic measurements made by the Mars Microphone by imposing
131 fluctuations of the pressure field in the vicinity of the instrument. These fluctuations will
132 depend on the position of SuperCam relative to the wind. Previous computational fluid dy-
133 namics simulations in the vicinity of the Perseverance vehicle ([Bardera-Mora et al., 2017](#))
134 have shown that the flow is attached upstream of the mast while the downstream velocity
135 field is strongly modified by the presence of the mast. A comprehensive understanding of the
136 interaction between the wind and the instrument could help to determine the wind's speed
137 and direction, which are of great interest to Mars atmospheric science. This study presents
138 the results of an experimental campaign conducted in a wind tunnel under a simulated Mar-
139 tian atmosphere with a full-scale model of the Perseverance mast equipped with microphones
140 and pressure sensors. It aims to explore the potential of the SuperCam microphone to retrieve
141 wind properties such as its speed and direction.

142 **2. Experimental configuration**

143 The wind calibration tests were conducted in the Aarhus Wind Tunnel Simulator II (AWT-
144 SII) in Denmark ([Holstein-Rathlou et al., 2014](#)). This facility can uniquely reproduce plane-
145 tary atmospheres. Specifically, it can simulate typical Mars surface conditions including a low
146 pressure CO₂ atmosphere with winds using a recirculating wind tunnel. It is also equipped
147 with a full set of internal sensors to monitor atmospheric parameters such as pressure, tem-
148 perature and humidity. The test campaign described in this paper was conducted at ambient

149 temperature ($\sim 23^\circ\text{C}$) and under a 10 mbar absolute pressure. This results in a 0.02 kg m^{-3}
150 atmospheric density, similar to Mars, which has typical temperatures ranging from -135°C
151 to 20°C and a mean atmospheric pressure around 6 mbar. A double square-meshed metallic
152 grid, with a wire spacing of 1 mm was placed at the middle of the tunnel to introduce a
153 controlled level of turbulence down to 10%. Considering an ideal gas law, these atmospheric
154 parameters lead to a speed of sound of 276 m s^{-1} inside the chamber.

155

156 To simulate as close as possible the flow generated around the SuperCam instrument, a
157 full-scale 3D-printed mock-up of the upper part of the *Perseverance* rover mast was mounted
158 inside the tunnel (Fig. 1a). It was equipped with three microphones (Knowles Electret con-
159 denser microphones, model EK-23132) that came from the same batch as the SuperCam
160 microphone flight model. The first one (front microphone) was placed in the same position
161 as the SuperCam instrument microphone, at the bottom left of the window. The second one
162 (side microphone) was located on the side of the Remote Warm Electronic Box (RWEB) that
163 covers SuperCam, and the last one (interior microphone) inside the RWEB, protected from
164 the wind flow (see Fig. 1 for the locations of the microphones). Two additional microphones
165 (upwind and downwind microphones) were placed in front of and behind the mock-up, re-
166 spectively, to study the upwind and downwind flow. Two barometers (Paroscientific absolute
167 pressure sensors, Model 215A-102) were also part of the mock-up payload: one at the bot-
168 tom right of the window (front barometer) and the other one on the side of the RWEB
169 (side barometer), below the microphone. A full schematic is shown in Fig. 1a and pictures
170 are provided in Figs 1b,c. This instrumented mast was attached to a rotating plate so that
171 its orientation could be changed relative to the wind flow. The SuperCam angle relative
172 to the wind is defined in Fig. 1d, with azimuthal angles increasing counterclockwise from
173 the direction of the flow. This will be used as the reference for data interpretation. The
174 positions of the upwind and downwind microphones were left unchanged during the entire
175 set of measurements.

176

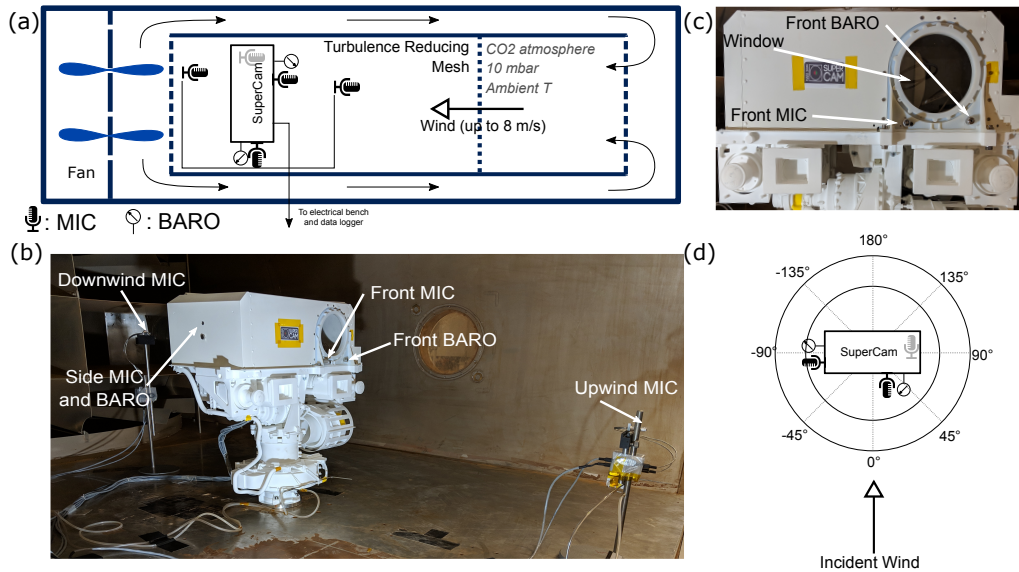


Figure 1: (a) Schematic of the SuperCam/Microphone wind calibration test set-up. (b) Photo of the Mars2020/SuperCam mast instrumented with microphones and barometers. (c) Close-up view of the Remote Warm Electronic Box (RWEB) equipped with a Mars Microphone and a barometer. (d) Definition of the SuperCam angle relative to the wind. MIC: Microphone, BARO: Barometer

177 Each microphone was connected to SuperCam-like front-end-electronics boards with two
 178 stages of amplification, providing an amplification factor of 62. The resulting sensitivity was
 179 1.4 V Pa^{-1} . The front-end-electronics were specifically adjusted for these tests to optimize
 180 the microphone bandwidth in the 10 Hz to 10 kHz frequency range. The microphone sam-
 181 pling frequency was set at 200 kHz. The barometric measurement system included the two
 182 absolute pressure transducers with their dedicated acquisition and processing boards. The
 183 measurement ranges were from 0 to 1 MPa in pressure and 0 to 100 Hz in bandwidth. A
 184 Beagle Bone Black board managed the configuration and the synchronous acquisition of
 185 the pressure sensors at a sampling rate of 200 Hz. It also acquired a synchronization signal
 186 generated by the microphone acquisition system to ensure the time consistency between the
 187 different recordings.

188

189 The mast was rotated in azimuth over 360° by steps of 15° , and over -15° to 15° in steps
 190 of 5° . This represents 30 different measurement angles. In chronological order, the mast was

191 rotated from 0° to 180° then from 0° to -180° . The elevation angle was 0° . For each angular
192 position of the mast and for 5 wind velocities of 0, 2, 4, 6 and 8 m s^{-1} , a 60s long recording
193 was simultaneously made for the five microphones and the two barometers. The maximum
194 wind speed was chosen to avoid saturation of the microphone electronics. Indeed, it will be
195 seen in the next section that the maximal amplitude of the raw signal that saturates the
196 microphones comes from a harmonic noise likely due to the rotor and that is three decade
197 higher in amplitude than the wind-induced signal (see Fig. 2). Therefore, the saturation will
198 not occur at this level with the flight model on Mars. Moreover, the amplification gain of the
199 flight-model microphone can be reduced down to a factor 30 leading to a saturation sound
200 pressure of about 4.5 Pa.

201

202 **3. Data processing: dealing with rotor fan noise**

203 Each microphone data point was converted into Pascals, considering the sensitivity of the
204 microphone and pressure sensors. The power spectrum for each acquisition was computed
205 and used for all of the following analyses.

206 Despite special precautions to reduce the wind generation system noise by mounting ex-
207 ternally the drive mechanism, some artificial noise propagates inside the tunnel. Moreover,
208 the steel and aluminum inner walls of the chamber resulted in significant sound reflections
209 (echoes). Therefore, a precise analysis of the noise components recorded inside the chamber
210 was needed in order to correctly interpret the results. For noise characterization, the results
211 of an additional static test (fixed microphones) with different microphone positions were also
212 used.

213

214 *3.1. Microphone Noise Spectrum Components*

215 Fig. 2a shows the typical noise spectra recorded by the front microphone and the interior
216 microphone. Both microphones measure a tonal noise with a low fundamental frequency and

Rotor (rpm)	Speed	Wind Speed (m/s)	Predicted Tonal Frequency (Hz)	Experimental Tonal Frequency (Hz)
202		2	44	44.2
406		4	88	88.6
548		6	119	119.5
711		8	154	155.1

Table 1: Rotation speed of the fan and the associated wind speed compared to the predicted tonal noise considering 13 fan blades ($f_b = \frac{RPM * N}{60}$ with N the number of blades Norton and Karczub (2003)) and the experimental frequency recorded in microphone spectra.

217 its associated harmonics. This tonal noise is considered to be induced by the rotor and is
218 the result of a non uniform flow interacting with blades, directly linked with blade passing
219 frequency (Neise and Michel, 1994). Table 1 shows the relationship between the rotation
220 speed of the fan and the fundamental frequency measured in the spectrum for the 4 tested
221 wind speeds. There is a linear correlation with a proportionality factor of 13.1 between the
222 rotor speed (in s^{-1}) and the experimental tonal frequency. It is directly linked with the 13
223 blades composing the fan. This confirms the rotor origin of these peaks (Norton and Karczub,
224 2003). For each acquisition, the fundamental frequency and the 25 following harmonics have
225 been filtered using a 12 Hz wide notch filter around each frequency peaks and all further
226 analyses in this study have been performed on filtered spectra (see Fig. 2b).

227

228 A comparison between the spectrum recorded by the interior microphone and the front
229 microphone, displayed in Fig. 2, shows that the noise power recorded inside the SuperCam
230 cover has the same amplitude as the spectrum recorded by the exterior microphone up to
231 100 Hz. Then the interior noise is more than one decade lower in amplitude between 100 Hz
232 and 2000 Hz. After 3000 Hz both spectra reach the noise floor, which is dominated by
233 electromagnetic noise. The spectrum recorded by the interior microphone displays more
234 bumps around harmonics whereas the spectrum from the front microphone is smoother and
235 does not follow the same trend, mainly in the 100 Hz to 2000 Hz frequency band. In addition
236 to the blade-induced tonal noise, this additional broadband noise was generated due to random
237 disturbances around blades such as turbulent boundary layer separation or vortex-induced

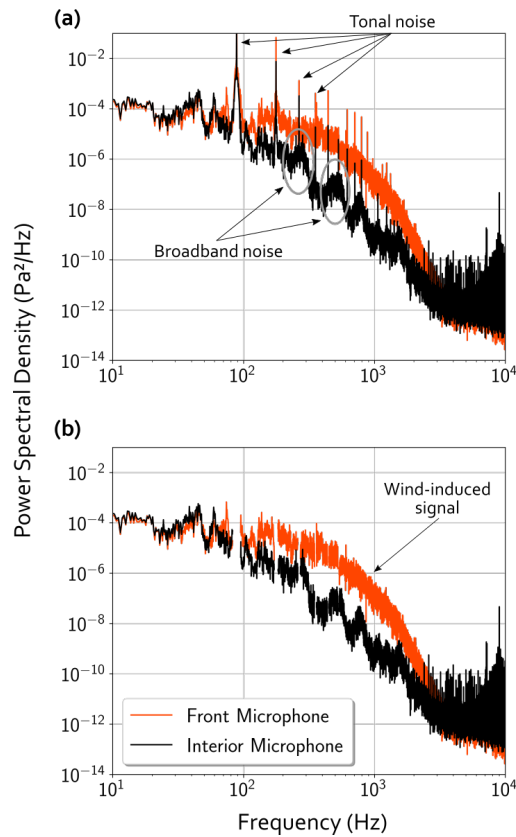


Figure 2: Comparison between acoustic power spectra recorded by the front microphone (orange) and the interior microphone (black) before filtering (a) and after filtering the fundamental and the 25 following harmonics (b). The fundamental and first harmonics peaks are highlighted by arrows. Broadband noise recorded by the interior microphone is highlighted by the grey circles. Spectra were acquired under a wind speed of 4 m s^{-1} and at SuperCam angle of 0 degree.

238 noise (Neise and Michel, 1994). Like the tonal noise, this aeroacoustic noise was recorded
 239 by both microphones. However, the front microphone which is unprotected outside the
 240 SuperCam mock-up, also recorded signal from the wind flowing past the microphone; the
 241 signal of interest for this study. Dynamic pressure affected the microphone membrane creating
 242 the wind-induced noise whereas the interior microphone was protected from the wind flow.
 243 Therefore, no wind-induced signal was recorded by the interior microphone. As a conclusion,
 244 the difference in amplitude between the interior microphone spectrum and front microphone
 245 spectrum is attributed to the dynamic pressure that creates the wind-induced signal on the
 246 front microphone membrane.

247 *3.2. Microphone Static Test*

248 An additional 'static' test was performed in order to complement the investigation of the
249 origin of the noise recorded by the microphones inside the chamber. Five microphones were
250 positioned facing the wind and at an increasing distance from a cubic obstacle (a speaker of
251 about $40\text{ cm} \times 70\text{ cm}$, installed for an other experiment not presented here). Therefore, the
252 microphones closest to the obstacle were partially shielded from the wind. The microphone
253 distances are referenced to the fan (downstream).

254 Synchronized acquisitions lasting 30s were performed for two different wind speeds,
255 4 m s^{-1} and 6 m s^{-1} . Fig. 3b shows the spectral energy of the tonal noise (spectral area
256 of the fundamental and 25 subsequent harmonics, top plot) as a function of the distance of
257 the microphone from the fan. Values are normalized by the spectral energy measured by the
258 microphone farthest from the obstacle (and therefore, closest to the fan). This comparison
259 shows that the tonal noise intensity is not correlated with the distance from the fan.

260 For the 4 m s^{-1} wind, energies at 5 m and 6 m from the fan are 1.8 times higher than the
261 one for the microphone closest to the fan. For the 6 m s^{-1} wind, energy at 5 m is 0.1 times
262 lower than the one for the microphone closest to the fan whereas the energy at 6 m is 1.3
263 times higher. The tonal noise is expected to be composed of a direct part, possibly coming
264 from both side (fan and recirculating wind tunnel), and a diffuse part due to the high acoustic
265 reflectivity of the chambers wall. The microphones recording a higher energy (respectively
266 a lower energy), may be due to anti-nodes (respectively nodes) of the chamber. The two
267 microphones closest to the obstacle record a lower value, possibly the consequence of an
268 attenuation due to the obstacle that may act as a screen for the direct field contribution.
269 The bottom plot in Fig. 3b shows the energy of the acoustic spectrum after filtering the
270 tonal noise. It does not follow the same variation as the tonal noise confirming that the origin
271 is different. The two microphones which are the farthest from the obstacle record the same
272 spectral energy as they are under the same wind flow at a constant speed. The 3 remaining
273 microphones, the closest to the obstacle, record a signal with a lower spectral energy. Due to
274 the shielding of the wind by the obstacle, the force of the wind that vibrates the microphone

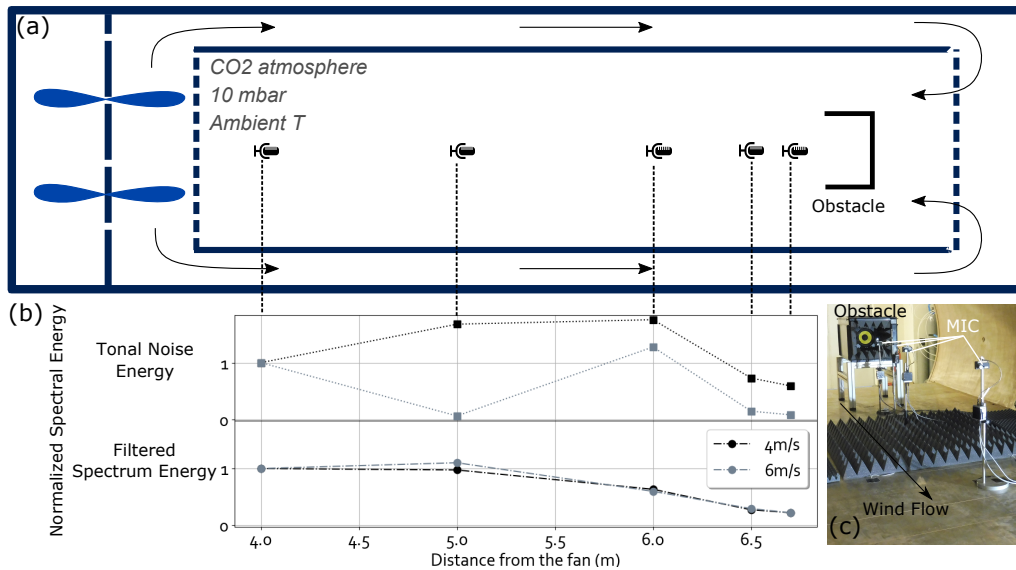


Figure 3: Schematic diagram of the static test used to confirm the wind origin of the noise recorded by exterior microphones. (a) 5 microphones were arranged facing the wind, behind an obstacle shielding the first microphones from the wind. (b) Spectral energy of the tonal noise (top) and of the filtered spectrum (bottom) for wind speeds of 4 m s^{-1} (black) and 6 m s^{-1} (grey). It is normalized by the energy measured by the microphone farthest from the obstacle. (c) View of the 4 first microphones and obstacle. Foam was installed for the purpose of another investigation, not related to this study.

275 membranes is lower. Therefore, the spectral energy recorded by those wind-shielded micro-
 276 phones is lower. This test confirms that the tonal noise originates from the fan and that the
 277 filtered signal is representative of the flow.

278

279 As a conclusion, three noise components can be distinguished in the microphone spectra:
 280 (1) a tonal noise that depends on the fan rotation speed, seen in all the spectra, that has a
 281 high amplitude but is easily filtered; (2) a broadband noise, only seen in the interior micro-
 282 phone spectra, which is lower in amplitude; (3) a wind-induced pressure fluctuation noise, as
 283 we will have on Mars, that dominates the tunnel-induced noise between 100 Hz and 2000 Hz
 284 (see annotations in Fig. 2 that show these three components). Moreover this static test,
 285 shows that this wind-induced pressure fluctuation noise varies when the microphone is par-
 286 tially protected from the wind. Therefore, we suggest that the filtered (tonal noise removed)
 287 microphone data can be used to perform analyses with regard to the wind speed.

289 4. Results and interpretation

290 4.1. Total Spectrum

291 Fig. 4 shows the power spectral density recorded by the front barometer and the front
 292 microphone for the four tested wind speeds. The spectrum for the barometer is displayed
 293 in the 0.1 Hz to 10 Hz frequency range and the spectrum for the microphone from 10 Hz to
 294 10 kHz. The spectra from the two instruments intersect at 10 Hz except in the case of a
 295 wind speed of 2 m s^{-1} where the barometer signal reaches the instrument noise floor between
 296 2 Hz and 10 Hz. For the microphone spectra, the signal reaches the noise floor at frequencies
 297 between 2000 Hz and 8000 Hz depending on the wind speed (see light grey lines in Fig. 4 that
 298 represent the no-wind noise floors of the two instruments, measured in the same conditions).
 299 The spectral amplitudes increase with the wind speed, and all exhibit a slowly decreasing
 300 amplitude from 0.1 Hz to ~ 500 Hz. The increasing spectral amplitude with the wind speed
 301 concurs with experimental spectra recorded in the infrasonic range presented in [McDonald](#)
 302 [and Herrin \(1975\)](#). Then, around 500 Hz, a slope change occurs and the spectra sharply
 303 decrease for all wind speeds. Given the difficulties in precisely determining the transition
 304 frequency, a median value of 500 Hz is assumed. Under a 2 m s^{-1} wind, the spectrum reaches
 305 the noise floor near 2000 Hz. For stronger wind speeds, the slope becomes even steeper above
 306 1500 Hz until it reaches the noise floor around 5000 Hz. Similar trends are also observed for
 307 the signals obtained from the barometer and microphone located on the side of the mock-up
 308 (not displayed here for the sake of conciseness).

309 The first portion of each spectrum, below 500 Hz, can be fitted with a power law f^b
 310 with b being the exponent slope (see colored straight lines in Fig. 4). The exponent slope is
 311 between -7.4×10^{-1} for 2 m s^{-1} and -3.0×10^{-1} for 8 m s^{-1} . Considering the frequency
 312 range of this decrease, it may be hypothesized empirically that this behavior is indicative
 313 of the inertial regime where the energy cascades from large-scale structures to smaller and
 314 smaller scale structures without dissipation. Above 500 Hz the spectrum falls off very steeply,

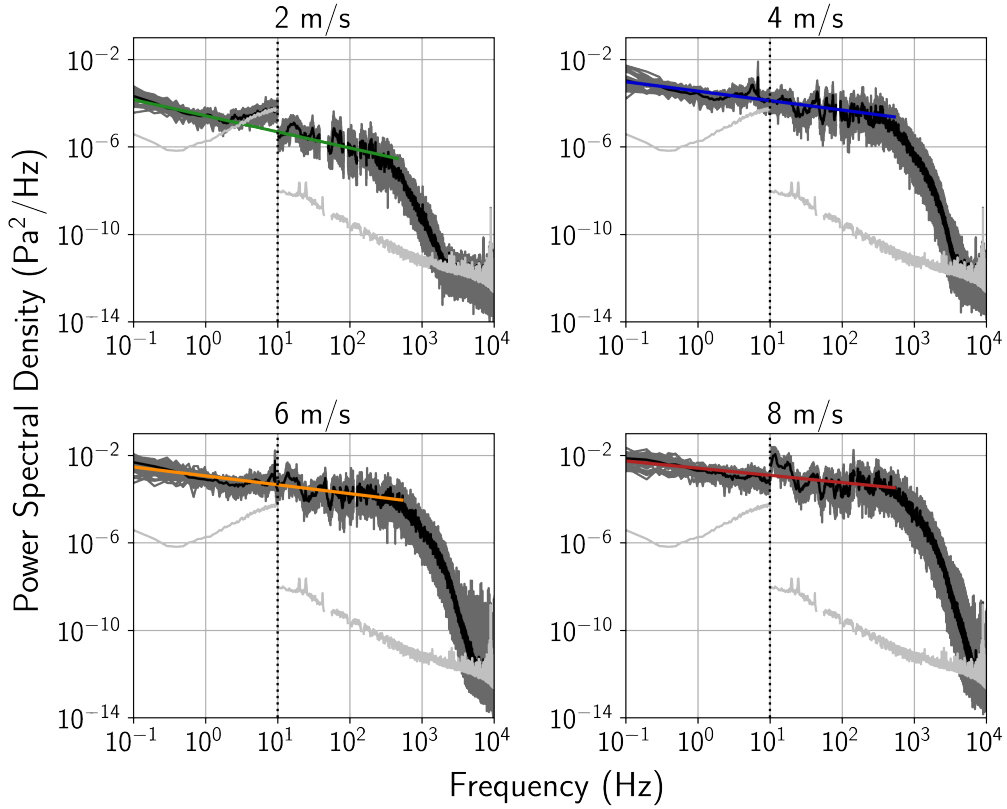


Figure 4: Power spectrum recorded by the front barometer (< 10 Hz) and microphone (> 10 Hz) for the 4 tested wind speeds. In each subplot, there are 30 dark grey spectra corresponding to the acquisitions at different SuperCam angles. The black curve is the median of these 30 spectra. The low frequency part of the spectra (below 500 Hz) is fitted by a power law ($f(x) = ax^b$ - colored lines). The light grey lines correspond to the no-wind noise floor of the barometer (left of vertical dashed line) and of the microphone (right of vertical dashed line)

315 possibly indicative of the dissipation regime where the viscosity strongly damps out the eddies
 316 and dissipates the energy.

317

318 In addition, the shaded area around the median spectra displayed in Fig. 4 show that there
 319 is a non-negligible dispersion of the frequency content with the microphone angle relative to
 320 the wind flow. Fig. 5 shows the 30 power spectra at different angles for a 6 m s^{-1} wind
 321 speed. Only the 100 Hz to 2000 Hz bandwidth is considered where the wind-noise magnitude
 322 is significantly larger than the chamber fan-induced noises (see section 3).

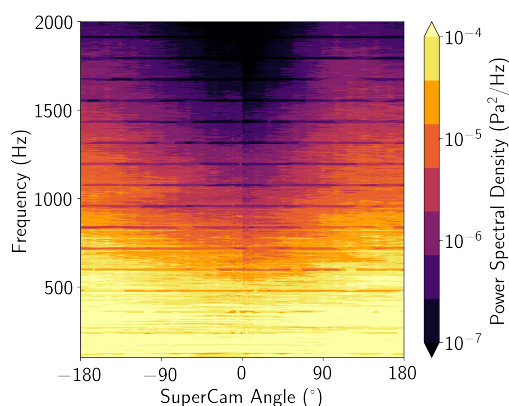


Figure 5: Power Spectral Density of the front microphone recorded for a wind speed of 6 m s^{-1} when rotating the mast around its axis. The 100 Hz to 2000 Hz frequency band is considered, as defined in Section 3. Other wind speeds follow the same behavior. Horizontal lines seen in the figure are areas where the tonal noise was removed. The slight discontinuity seen at 0° comes from two measurements performed at this angle.

323 This figure shows that the spectra for all instrument orientations have the same amplitude
 324 up to ~ 500 Hz, the end of the first (possibly inertial) regime. However, at the end of the first
 325 regime, when the sharp decrease in amplitude starts, the instrument orientation influences
 326 the spectral amplitude.

327 4.2. Link between the microphone signal and wind properties

328 Detailed analysis of microphone spectra shows that the lower-frequency part (typically
 329 below 500 Hz) is less influenced by the orientation of the instrument relative to the wind than
 330 higher frequencies. Moreover, the magnitude of the first regime is observed to increase with
 331 wind speed. On the other hand, an influence of the angle between the instrument and the
 332 wind is visible in the higher frequency (typically above 500 Hz) content of the spectra. For the
 333 subsequent analyses, the power spectrum is therefore separated into two frequency domains
 334 of interest considering the transition seen around 500 Hz: the 'low frequency' regime ranging
 335 from 100 Hz to 500 Hz and the 'high frequency' regime, ranging from 500 Hz to 2000 Hz.
 336 This allows the behaviors of the lower frequency domain and the higher frequency domain to
 337 be studied with respect to both the wind speed and wind orientation.

338 As microphones only measure pressure fluctuations around the mean value, the root mean
 339 square (RMS) of the pressure in a dedicated frequency band is used for the following analysis.

340 The RMS of the pressure is given as the square root of the power spectrum area in a chosen
341 frequency band between f_1 and f_2 :

$$\text{RMS Pressure} = \sqrt{\int_{f_1}^{f_2} \text{PSD}(f) df} \quad (1)$$

342 where $\text{PSD}(f)$ is the power spectral density at the frequency f . The RMS of the pressure
343 is then computed over the two frequency bands highlighted in the analysis of Fig. 5, from
344 100 Hz to 500 Hz and from 500 Hz to 2000 Hz.

345

346 Fig. 6 displays the front microphone RMS pressure integrated over the 100 Hz to 500 Hz
347 frequency band, as a function of the wind speed imposed in the tunnel. For each wind speed,
348 a dispersion with the angle of $\pm 10\%$ ($\pm 1\sigma$) around the mean value is noticed. As it was
349 inferred from the level of the first regime in Fig. 4, the microphone RMS pressure increases
350 with the wind speed and can be fitted using a parabolic model. For a wind speed of 2 m s^{-1}
351 the model overestimates the RMS pressure whereas it matches the RMS pressure within its
352 dispersion interval for wind speeds higher than 3 m s^{-1} . The discrepancy at low wind speed
353 may be due to uncontrolled upstream conditions of the tunnel. This plot shows that the RMS
354 pressure is proportional to the wind-induced dynamic pressure. As a consequence, monitoring
355 the microphone RMS pressure on Mars can be used to evaluate the wind speed.

356 The dispersion of the measurements with the angle of the microphone relative to the wind
357 means that there will be an uncertainty in the determination of the wind speed: $\pm 0.4 \text{ m s}^{-1}$
358 for a wind speed of 4 m s^{-1} and $\pm 0.6 \text{ m s}^{-1}$ for a wind speed of 8 m s^{-1} . Previous Earth
359 atmosphere studies observed a quadratic correlation between sound pressure fluctuation and
360 average wind velocity (Strasberg, 1988; Morgan and Raspert, 1992). However, this quadratic
361 model is no longer valid (the exponent of the speed becomes higher than 2) when the orien-
362 tation of the microphone is changed or when the turbulence of the incident air flow increases.
363 The latter could also explain why the point at 2 m s^{-1} does not match the parabolic model.

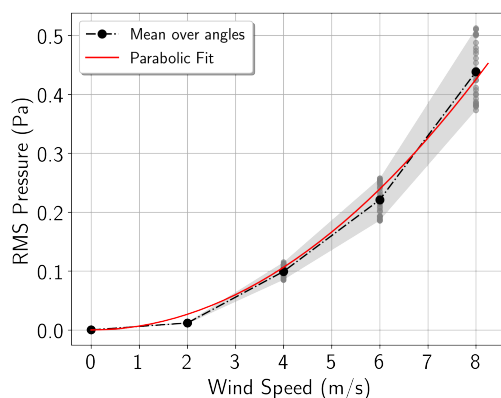


Figure 6: Front Microphone RMS Pressure over the 100 Hz to 500 Hz frequency band as a function of the upstream wind speed in the tunnel. Grey points are values computed for the 30 SuperCam angles. The shaded zone is delimited as the area between the minimal and maximal value for each speed. The black dashed curve represents the mean value over those 30 points. The red solid curve is the best fit to the data with a parabolic model $f(x) = ax^2$, with $a = 6.6 \times 10^{-3}$

364

365 The influence of the microphone angle relative to the wind is much more important in the
 366 500 Hz to 2000 Hz frequency range. Fig. 7 shows the evolution of the RMS pressure over this
 367 frequency range as a function of the microphone angle relative to the axis of the tunnel. For
 368 each microphone, the 0° angle corresponds to the position of the mast where the microphone
 369 is pointing towards the upstream part of the tunnel, corresponding to a SuperCam angle
 370 of 0° for the front microphone and a SuperCam angle of 90° for the side microphone (see
 371 central schematics in the diagram in Fig. 7). Incident wind is theoretically coming from this
 372 direction. For display purposes, the RMS pressure at each wind speed, is normalized by the 0°
 373 value. It can be seen that for all upstream wind velocities, the RMS pressure varies by $\pm 27\%$
 374 ($\pm 1\sigma$) around the mean value over the 30 pointing angles of the mast. This dispersion with
 375 angle is much larger than the $\pm 10\%$ previously highlighted over the lower frequency band,
 376 quantitatively confirming the previous inferences from Fig. 5. In addition, it is observed that
 377 the RMS pressure reaches a minimum when the microphone is approximately facing the wind,
 378 whereas it reaches a maximum when the microphone is facing downwind (see polar plots in
 379 Fig. 7 and linear representation at one wind velocity in Fig. 8).

380 First, it is noticed that the increase of the RMS pressure from its minimum value is steeper

381 for the front microphone than for the side microphone. The later shows a flat plateau around
382 the minimum (see Fig. 8b). RMS pressure has increased by 10% at $\pm 30^\circ$ from the minimum
383 angle for the front microphone whereas it has increased by 10% at $\pm 60^\circ$ from the minimum
384 angle for the side microphone. Indeed the front microphone is located on a larger surface
385 than the side microphone. When this larger surface is facing the wind it results in a blockage
386 effect of the flow inside the wind tunnel that modifies it in the close vicinity of the mock-up.
387 The larger the surface facing the wind is, the more important this effect. Moreover, the side
388 microphone is located on a flat and smooth surface whereas the front microphone is located
389 below the window close to many centimeter scale obstacles (see Figs. 1b and 1c). A slight
390 rotation of the mast leads to these small obstacles interacting with the wind flow. This will
391 favor flow separation and vortex generation, in turn increasing the RMS pressure recorded by
392 the front microphone. For the side microphone, because of the lack of hurdles around the
393 microphone, the flow separates at higher angles.

394
395 The evolution of the RMS pressure as a function of the angle is fitted with a subcar-
396 dioid curve ($f(\theta) = a + b\cos(\theta - \theta_0)$) for all the wind speeds and both microphones. It is
397 represented in Fig. 8a for the front microphone and in 8b for the side microphone. The
398 shaded area represents the 95% interval of confidence of the fit. For the side microphone,
399 the subcardioid model does not fit with points around the minimum value because of the
400 aforementioned plateau. However, the model works for points with values $> 110\%$ of the
401 minimum value. Hence, for both microphones and for all the wind speeds, the angle where
402 the RMS pressure is minimum is estimated as the θ_0 parameter returned from the subcardioid
403 fit. Results are presented in Table 2. It is assumed that the axis defined between the angle
404 where the microphone RMS pressure is minimal and the angle where the microphone RMS
405 pressure is maximal corresponds to the incident wind direction. Indeed, the situation can be
406 compared with Von Karman vortex streets created in the wake of a cylindrical object. When
407 the microphone is rotated away from the direction facing into the wind, the flow progressively
408 separates, generating vortices that enrich the spectral content of the acoustic pressure fluctu-

	Front Microphone	Side Microphone
2 m/s	$-11.4^\circ \pm 4.0^\circ$	$-18.4^\circ \pm 4.0^\circ$
4 m/s	$-8.7^\circ \pm 2.4^\circ$	$-18.0^\circ \pm 4.0^\circ$
6 m/s	$-7.3^\circ \pm 3.1^\circ$	$-17.0^\circ \pm 2.5^\circ$
8 m/s	$-13.5^\circ \pm 3.3^\circ$	$-17.4^\circ \pm 2.9^\circ$

Table 2: Measured angular positions of the microphones relative to the wind where the RMS pressure is minimum. This angle is returned from the fit of the RMS pressure with a subcardioid law (see Fig. 8). Error is computed as the 95% confidence interval on the estimation of this parameter.

409 ations. When the microphone is rotated downwind (*i.e.* angles around 180°), it is immersed
410 in a massively separated flow region in the wake of the instrument where small vortices are
411 numerous.

412 Both microphone record wind orientation that has a negative offset from the 0° position.
413 For the front microphone, the minimum RMS pressure is reached at an angle between -13.5°
414 and -7.3° depending on the wind speed. For the side microphone the minimum RMS pres-
415 sure is reached at an angle between -18.4° and -17.4° , which is between 4° and 10° lower
416 than angles determined for the front microphone. The retrieved wind direction is represented
417 in Fig. 7 as the straight colored lines for each wind speed. This lower offset for the front
418 microphone compared to the side microphone can result from the asymmetry of the front
419 microphone position with respect to the center of the tunnel which is positioned a little closer
420 to the left edge of the SuperCam cover, but also asymmetries of the SuperCam cover itself
421 that lead to a small bias in the determination of the angle. Nevertheless, the negative offset
422 from the 0° position retrieved for both microphones is attributed to an upstream velocity
423 vector which is not perfectly aligned with the axis of the tunnel. Furthermore, for each wind
424 speed, considering the lower bound of the uncertainty interval for the front microphone and
425 the upper bound of the uncertainty interval for the side microphone, it results in a wind
426 direction that can be estimated with an uncertainty of $\pm 10^\circ$.

427

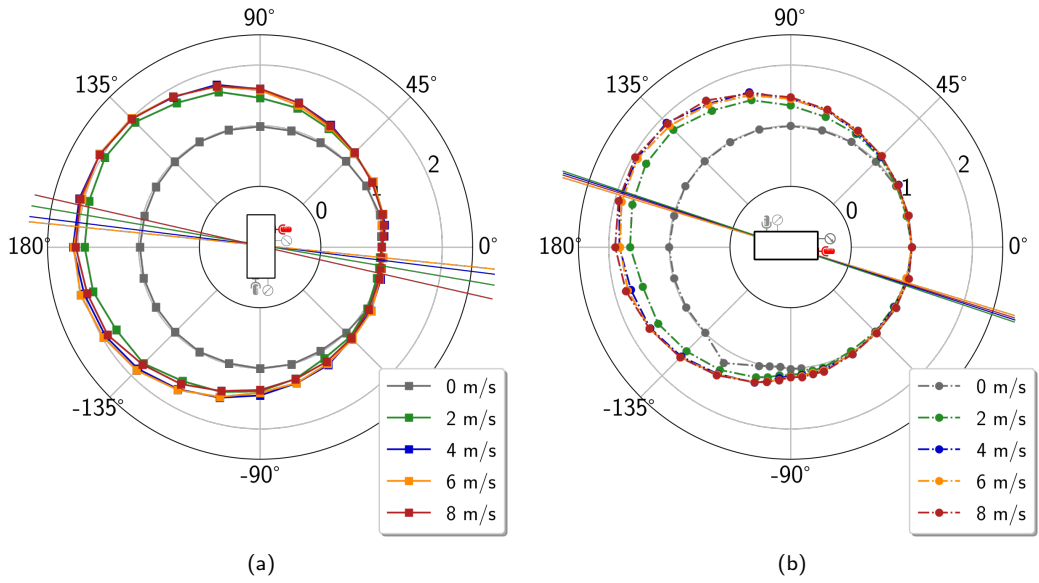


Figure 7: Normalized RMS pressure over the 500 Hz to 2000 Hz frequency range for the front microphone (a) and for the side microphone (b) as a function of the microphone angle relative to the tunnel axis. For both plots, 0° position corresponds to the scheme in the inner part of the diagram. Straight colored lines represent the wind direction estimated from Table 2.

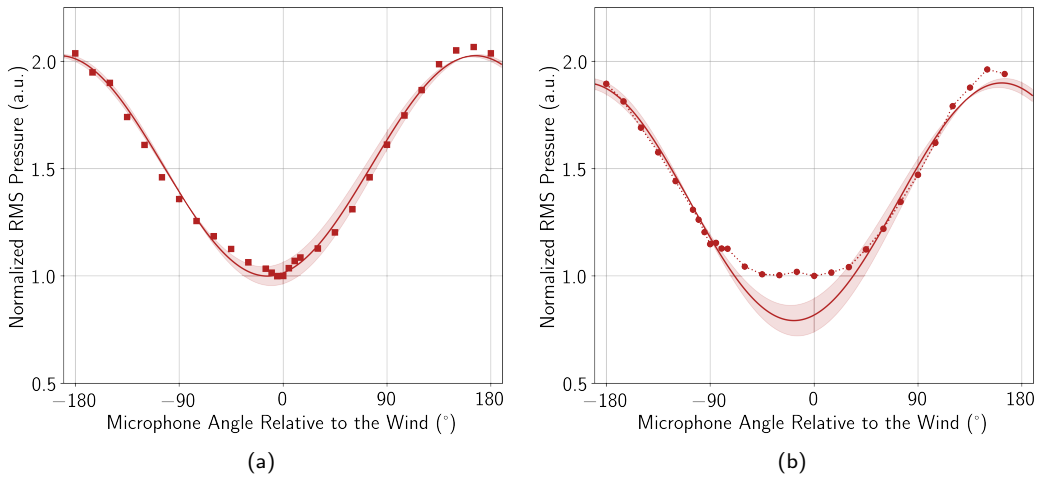


Figure 8: Determination of the angles where the RMS pressure is minimum and maximum for the front microphone (a) and for the side microphone (b) and for a wind speed of 8 m s^{-1} . Normalized measured RMS Pressure as a function of the wind incident angle relative to the microphone is represented by colored points (same data as Fig. 7). The experimental points are fitted with a subcardioid $f(\theta) = a + b\cos(\theta - \theta_0)$ to determine the angular position of the minimum and the maximum. The shaded area represent the 95% interval of confidence of the fit. Other wind speeds are not represented but behaviors are the same.

428 5. Discussion

429 5.1. Comparison with previous studies

430 Audible noise has not yet been studied on Mars nor, to our knowledge, in a simulated
431 Martian environment with the exception of the proof-of-concept study presented in [Lorenz
432 et al. \(2017\)](#). Surprisingly, direct comparisons of the influence of wind direction on the audible
433 noise level can be found in hearing-aid literature. [Zakis \(2011\)](#) presented the results of a wind-
434 tunnel experimental campaign focusing on the influence of wind speed and azimuth on noise
435 of hearing-aids positioned in a mock-up of a human head. An increase of the wideband
436 noise with wind speed is also observed, but its evolution with the wind incidence angle is
437 more difficult to interpret. In their study, clear minimum values are seen at all wind speeds
438 when microphones were facing the wind, similar to our Martian study. They find that the
439 wind noise is at its maximum when microphones are pointing rearward for a wind speed of
440 12 m s^{-1} (the strongest wind speed that they studied), however, this is not reproducible for
441 other conditions. The behavior with varying angle is more difficult to interpret because of the
442 specificity of microphone integration with regard to the head and ear. In a comparable study,
443 [Chung et al. \(2009\)](#) also includes a comparison with a less complex case of a microphone
444 mounted on the surface of a cylinder. This study confirms that the lowest wind noise is
445 observed when the microphone is facing the wind and the highest wind noise is observed
446 when the microphone is facing downstream. This transition from minimum wind noise is
447 to maximum wind noise when rotating the cylinder by 180° is explained by the turbulence
448 induced by the separation of the air flow in the wake of the cylinder. Therefore, it supports
449 the findings presented in this Martian study.

450 5.2. First comparison with Direct Numerical Simulations of the flow past SuperCam

451 In an attempt to unravel the flow structure past the SuperCam instrument as a function
452 of the direction and velocity of the wind on Mars, a series of direct numerical simulations
453 (DNS) has been performed. The three-dimensional time-dependent Navier-Stokes equations

454 around a simplified model of the full-scale SuperCam instrument were directly solved using
 455 an Eulerian finite volume method. Assuming incompressible viscous flow, the equations read:

$$\vec{\nabla} \cdot \vec{v} = 0 \quad (2a)$$

$$\frac{\partial \vec{v}}{\partial t} + (\vec{v} \cdot \vec{\nabla}) \vec{v} = -\frac{1}{\rho} \vec{\nabla} p + \nu \nabla^2 \vec{v} \quad (2b)$$

456 where \vec{v} is the velocity, p the pressure, ρ and ν the fluid density and kinematic viscosity,
 457 respectively. The fluid properties are set with respect to the Martian environmental properties.
 458 The gas is pure CO₂. Its density, pressure and kinematic viscosity are set to 0.02 kg m⁻³,
 459 6 mbar and 6.9×10^{-4} m² s⁻¹, respectively (corresponding to an air temperature of 210 K).
 460 The model of SuperCam, of width L , is enclosed in a cylindrical computational domain of
 461 diameter $40L$ and of height $12L$. It is centered on the vertical axis of the cylinder and
 462 its altitude, relative to the ground, is fixed similar to its actual height on the rover. The
 463 coordinates origin is located at the geometrical center of the instrument.

464 The surface of SuperCam and the lower flat surface of the computational cylinder, which
 465 represents the ground, are modeled as non-slip surfaces. A velocity Dirichlet condition is im-
 466 posed on the tubular and on the upper flat surfaces of the computational domain, to represent
 467 the freestream Martian wind. This permits the direction and velocity of the wind relative
 468 to the instrument to be changed easily while ensuring a uniform boundary condition. Here
 469 the freestream wind velocity U_∞ has been set to 1 m s⁻¹, 3 m s⁻¹ and 5 m s⁻¹, respectively.
 470 The corresponding Reynolds numbers Re_L , based on the width L of SuperCam and on U_∞ ,
 471 range from 725 to 3620. These low Reynolds numbers justify the DNS approach. For each
 472 wind speed, its direction β was altered in 45° increments, from $\beta = 0^\circ$ (the microphone is
 473 facing the wind, Fig. 9a) to $\beta = \pm 180^\circ$ (the microphone is facing away from the wind).

474 The computational domain is composed of 8 million polyhedral cells. It is highly refined
 475 close to and in the wake of SuperCam (Fig. 9b). The mesh refinement zones are thus adapted
 476 depending on the direction of the wind, to capture the wake (see Fig. 9c). This results in

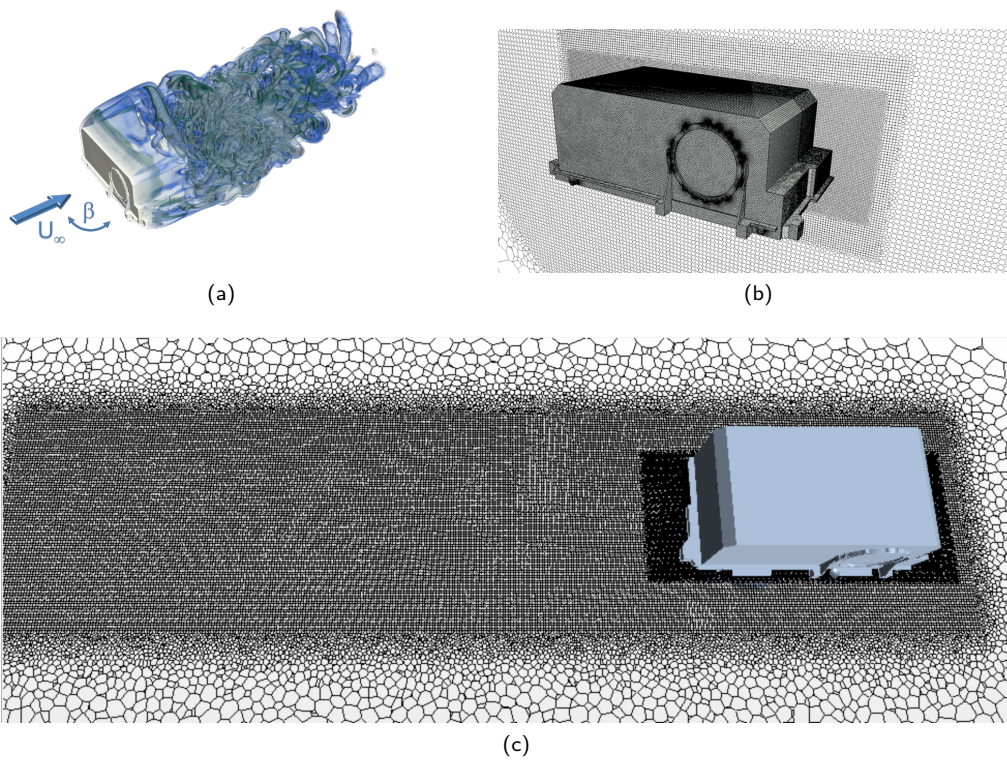


Figure 9: (a) Illustration of the freestream wind parameters U_∞ and β and the resulting vortices in the wake. (b) Close view of the polyhedral mesh around the SuperCam, here for the flow configuration with the microphone facing the wind ($\beta = 0^\circ$). (c) View of the refined mesh in the wake of SuperCam. Here the wind is flowing from the right to the left, with $\beta = -90^\circ$. For the sake of clarity, the surface mesh on the model of SuperCam is not depicted.

477 local, cell-based Reynolds numbers close to a few units in these refined zones.

478 The spatial and temporal discretizations are achieved using second-order upwind schemes
479 and second-order implicit time-stepping method respectively. The pressure velocity coupling
480 is obtained using the SIMPLE algorithm. The time step is fixed in order to satisfy the CFL
481 condition (Courant Number close to unity), regardless of the flow conditions.

482 Further simulations (not discussed here) were carried out to ensure that the results are
483 independent of the number of cells, the time step and the position of the external boundary
484 conditions.

485

486 The analysis of the flow is based on the spatio-temporal evolution of the near-wake vor-
487 tical structures, identified in terms of iso-surfaces of λ_2 -criterion (Jeong and Hussain, 1995;
488 Bury and Jardin, 2012), and their impact on the unsteady pressure field exerted on the mi-
489 crophone. Here the analysis focuses on a freestream wind velocity of 5 m s^{-1} . The numerical
490 results reveal the occurrence of complex instability modes in the close wake of SuperCam,
491 depending on the direction of the wind. Fig.10 depicts the vortical structures in the wake of
492 SuperCam for a 5 m s^{-1} Martian wind when the wind direction is varied from 0° to $\pm 180^\circ$.
493 The wake features very different shapes and different spreading of the size of the vortices as
494 the instrument is progressively rotated 360° .

495

496 An analysis of the time histories of the pressure signal measured at the location of the
497 SuperCam Microphone will be part of a subsequent study. It is expected that, as observed
498 experimentally, the direction of the wind impacts both the mean and fluctuating values of the
499 pressure signal at the location of the microphone with the RMS value providing more detailed
500 information on both the wind direction and velocity. It should also be possible to identify the
501 vortex shedding frequency peak as the SuperCam is rotated. This additional information can
502 likely be used to determine the Martian wind speed and direction *in situ* using the SuperCam
503 Microphone.

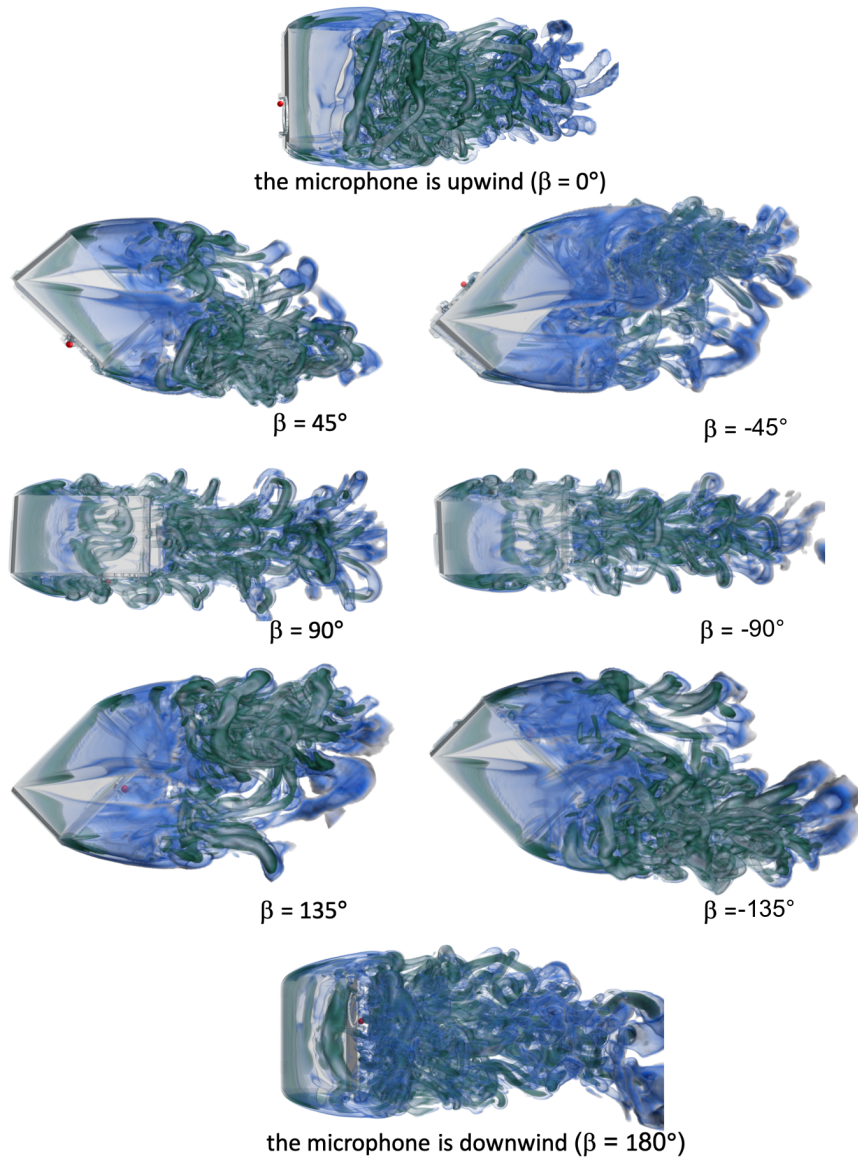


Figure 10: Iso-surfaces of λ_2 -criterion, revealing the vortical structures in the wake of the SuperCam instrument (upper view), for a 5 m s^{-1} wind flowing from left to right, as its direction relative to SuperCam is rotated 360° . SuperCam angles are indicated below each figure. The different colors correspond to more or less (dark green to light blue) intense vortices. The red dot illustrates the SuperCam microphone flight-model location.

504 5.3. Weaknesses and perspectives

505 This test campaign was conducted in the best facility to simulate a Mars wind flow on a
506 real scale model of the SuperCam microphone integrated in a full-scale mock-up of the upper
507 part of the *Perseverance* rover mast. However this experimental flow cannot be approximated
508 as a free field due to the inability for tunnels to host eddy sizes and length scales that are
509 present in the Mars boundary layer. Therefore, low frequency turbulence that occurs on Mars
510 (time scale longer than 1 s, [Smith et al. \(2004\)](#)) is not represented in this wind tunnel but are
511 not likely to be measured by the microphone flight model that has a response time starting at
512 100 Hz. Moreover, this experimental flow is subject to artifacts associated to closed tunnels
513 that can lead to not perfectly controlled upstream conditions and a slightly flapping flow.
514 For instance, the negative offset found for the retrieved wind direction ([Fig. 7](#)) highlights
515 these experimental bias. However, although the noise associated with the engine has been
516 filtered out (see [Section 3](#)), we can expect that the microphone spectrum integrates signal
517 induced by interactions between the wind and other components of the tunnel. Therefore,
518 a cross calibration on Mars with the MEDA instrument is strongly recommended to confirm
519 the trend observed for the RMS pressure as function of both the wind speed and direction
520 and also to compare between experimental, simulated and *in situ* conditions. In term of Mars
521 operations, if the subcardiod model used to represent the evolution of the RMS pressure
522 over a 360° rotation is confirmed by this suggested cross calibration, only one recording at
523 three azimuth pointing angles spaced by 120° will be necessary to constrain the parameters
524 of the subcardiod and therefore, determine the wind direction. Furthermore, as shown in
525 [Bardera-Mora et al. \(2017\)](#), the wind velocity measured at the microphone's location may be
526 lower than the actual mean wind speed, because of flow stagnation immediately upwind of
527 the instrument. The cross-calibration with MEDA, which does not seem to be sensitive to
528 this effect, would allow the calibration of the microphone RMS pressure with respect to the
529 true wind speed.

530 6. Conclusion

531 The SuperCam Microphone, located at the top of the mast of the Mars 2020 Perseverance
532 rover will record for the first time audio signal from the surface of Mars in the audible range.
533 In preparation for surface operations, and scientific analyses of the data, this paper presents an
534 experimental study of the wind-induced noise on the SuperCam Microphone under controlled
535 Mars air-pressure conditions.

536 Acoustic spectra from 100 Hz to 10 kHz display a low frequency regime (< 500 Hz) whose
537 amplitude increases as a function of the average wind speed squared. At higher frequencies,
538 the spectral energy sharply dissipates and the RMS pressure at frequencies higher than 500 Hz
539 presents a minimum value when the microphone is facing the wind and a maximal value when
540 the microphone is pointing downwind. Therefore, recording the Martian acoustic pressure
541 fluctuations with the microphone when SuperCam is rotated in azimuth around its mast is
542 a way to determine *in situ* the Martian wind vector with an uncertainty of $\pm 1 \text{ m s}^{-1}$ on
543 speed and $\pm 10^\circ$ on the orientation. The identification of where the high-frequency RMS
544 pressure is minimum and maximum gives the wind direction while the RMS pressure at lower
545 frequencies can be used to determine the wind speed.

546 However, as inferred from previous Earth atmosphere studies ([Strasberg, 1988](#); [Morgan](#)
547 [and Raspet, 1992](#)), the RMS pressure depends on the level of intrinsic turbulence of the
548 wind flow. The wind tunnel used for this experiment does not reproduce levels of turbulence
549 achieved on Mars. Therefore, a cross-calibration with MEDA, the Perseverance weather sta-
550 tion, is required after landing. Simultaneous measurement with MEDA and the SuperCam
551 microphone will help to draw the calibration curve of RMS pressure as a function of the Mars
552 wind speed. Measurements over a full 360° in azimuth are needed to determine the wind
553 orientation. A calibration run performed in parallel with MEDA is also suggested in order to
554 demonstrate *in situ* the results presented in this study, but also to explore the influence of the
555 elevation angle that has not been tested here. Furthermore, the measurement of the acous-
556 tic power spectrum will complement in higher frequencies the pressure fluctuation spectrum
557 recorded by APSS/Insight. The early development of a numerical model shows a different

558 behavior of the flow whether the microphone is facing the wind or pointing downwind. Future
559 ongoing studies will help to better understand the interaction of the flow with the body of
560 the rover.

561

562 Considering these experimental results, the SuperCam Microphone has *a priori* the po-
563 tential to determine both the wind speed (from the low-frequency component) and the wind
564 incident angle (from the high frequency component) on Mars. Therefore, in addition to
565 being valuable for Laser Induced Breakdown Spectroscopy investigation (Chide et al., 2019;
566 Murdoch et al., 2019), it will also contribute to Martian atmospheric science investigations.

567 **7. Acknowledgements**

568 This work was funded by CNES and Région Occitanie as part of a PhD thesis. We
569 gratefully acknowledge funding from Europlanet. Europlanet 2020 RI has received funding
570 from the European Union's Horizon 2020 research and innovation programme under grant
571 agreement No 654208.

572 **References**

- 573 Balme M, Greeley R. Dust devils on earth and mars. *Reviews of Geophysics* 2006;44(3). doi:[10.1029/](https://doi.org/10.1029/2005rg000188)
574 [2005rg000188](https://doi.org/10.1029/2005rg000188).
- 575 Banerdt WB, Smrekar SE, Banfield D, Giardini D, Golombek M, Johnson CL, Lognonné P, Spiga A, Spohn
576 T, Perrin C, Stähler SC, Antonangeli D, Asmar S, Beghein C, Bowles N, Bozdog E, Chi P, Christensen U,
577 Clinton J, Collins GS, Daubar I, Dehant V, Drilleau M, Fillingim M, Folkner W, Garcia RF, Garvin J, Grant J,
578 Grott M, Grygorczuk J, Hudson T, Irving JCE, Kargl G, Kawamura T, Kedar S, King S, Knapmeyer-Endrun
579 B, Knapmeyer M, Lemmon M, Lorenz R, Maki JN, Margerin L, McLennan SM, Michaut C, Mimoun D,
580 Mittelholz A, Mocquet A, Morgan P, Mueller NT, Murdoch N, Nagihara S, Newman C, Nimmo F, Panning
581 M, Pike WT, Plesa AC, Rodriguez S, Rodriguez-Manfredi JA, Russell CT, Schmerr N, Siegler M, Stanley
582 S, Stutzmann E, Teanby N, Tromp J, van Driel M, Warner N, Weber R, Wieczorek M. Initial results from
583 the InSight mission on mars. *Nature Geoscience* 2020;13(3):183–9. doi:[10.1038/s41561-020-0544-y](https://doi.org/10.1038/s41561-020-0544-y).
- 584 Banfield D, , Rodriguez-Manfredi JA, Russell CT, Rowe KM, Leneman D, Lai HR, Cruce PR, Means JD, John-
585 son CL, Mittelholz A, Joy SP, Chi PJ, Mikellides IG, Carpenter S, Navarro S, Sebastian E, Gomez-Elvira J,
586 Torres J, Mora L, Peinado V, Lepinette A, Hurst K, Lognonné P, Smrekar SE, Banerdt WB. InSight auxil-
587 iary payload sensor suite (APSS). *Space Science Reviews* 2018;215(1). doi:[10.1007/s11214-018-0570-x](https://doi.org/10.1007/s11214-018-0570-x).
- 588 Banfield D, Spiga A, Newman C, Forget F, Lemmon M, Lorenz R, Murdoch N, Viudez-Moreiras D, Pla-Garcia
589 J, Garcia RF, Lognonné P, Özgür Karatekin , Perrin C, Martire L, Teanby N, Hove BV, Maki JN, Kenda B,
590 Mueller NT, Rodriguez S, Kawamura T, McClean JB, Stott AE, Charalambous C, Millour E, Johnson CL,
591 Mittelholz A, Määttänen A, Lewis SR, Clinton J, Stähler SC, Ceylan S, Giardini D, Warren T, Pike WT,
592 Daubar I, Golombek M, Rolland L, Widmer-Schmid R, Mimoun D, Beucler É, Jacob A, Lucas A, Baker
593 M, Ansan V, Hurst K, Mora-Sotomayor L, Navarro S, Torres J, Lepinette A, Molina A, Marin-Jimenez M,
594 Gomez-Elvira J, Peinado V, Rodriguez-Manfredi JA, Carcich BT, Sackett S, Russell CT, Spohn T, Smrekar
595 SE, Banerdt WB. The atmosphere of mars as observed by InSight. *Nature Geoscience* 2020;13(3):190–8.
596 doi:[10.1038/s41561-020-0534-0](https://doi.org/10.1038/s41561-020-0534-0).
- 597 Bardera-Mora R, Sor S, Garcia-Magariño A, Gomez-Elvira JJ, Marin M, Torres J, Navarro S, Carretero S.
598 Characterization of the flow around the mars 2020 rover. In: 35th AIAA Applied Aerodynamics Conference.
599 American Institute of Aeronautics and Astronautics; 2017. doi:[10.2514/6.2017-4228](https://doi.org/10.2514/6.2017-4228).
- 600 Bass HE, Raspet R, Messer JO. Experimental determination of wind speed and direction using a three
601 microphone array. *The Journal of the Acoustical Society of America* 1995;97(1):695–6. doi:[10.1121/1.](https://doi.org/10.1121/1.412293)
602 [412293](https://doi.org/10.1121/1.412293).
- 603 Bury Y, Jardin T. Transitions to chaos in the wake of an axisymmetric bluff body. *Physics Letters A*
604 2012;376(45):3219–22. doi:[10.1016/j.physleta.2012.09.011](https://doi.org/10.1016/j.physleta.2012.09.011).
- 605 Chide B, Maurice S, Mimoun D, Murdoch N, Lorenz R, Wiens R. Speed of Sound Measurements on Mars and
606 its Implications. In: 51st Lunar and Planetary Science Conference. The Woodlands, TX, United States;

607 2020. p. 1366.

608 Chide B, Maurice S, Murdoch N, Lasue J, Bousquet B, Jacob X, Cousin A, Forni O, Gasnault O, Meslin PY,
609 Fronton JF, Bassas-Portús M, Cadu A, Sournac A, Mimoun D, Wiens RC. Listening to laser sparks: a
610 link between laser-induced breakdown spectroscopy, acoustic measurements and crater morphology. *Spectrochimica Acta Part B: Atomic Spectroscopy* 2019;153:50–60. doi:[10.1016/j.sab.2019.01.008](https://doi.org/10.1016/j.sab.2019.01.008).

612 Chung K, Mongeau L, McKibben N. Wind noise in hearing aids with directional and omnidirectional microphones: Polar characteristics of behind-the-ear hearing aids. *The Journal of the Acoustical Society of America* 2009;125(4):2243–59. doi:[10.1121/1.3086268](https://doi.org/10.1121/1.3086268).

615 de la Torre Juarez M, Rodrigez-Manfredi J, Apestigue V, Banfield D, Boland J, Conrad P, the MEDA Team
616 . Performance after the Integration of MEDA, the Environmental and Meteorological Package for Mars
617 2020. In: 51st Lunar and Planetary Science Conference. The Woodlands, TX, United States; 2020. p.
618 2971.

619 Hess SL, Henry RM, Leovy CB, Ryan JA, Tillman JE. Meteorological results from the surface of mars: Viking
620 1 and 2. *Journal of Geophysical Research* 1977;82(28):4559–74. doi:[10.1029/js082i028p04559](https://doi.org/10.1029/js082i028p04559).

621 Holstein-Rathlou C, Gunnlaugsson HP, Merrison JP, Bean KM, Cantor BA, Davis JA, Davy R, Drake NB,
622 Ellehoj MD, Goetz W, Hviid SF, Lange CF, Larsen SE, Lemmon MT, Madsen MB, Malin M, Moores JE,
623 Nørnberg P, Smith P, Tamppari LK, Taylor PA. Winds at the phoenix landing site. *Journal of Geophysical Research* 2010;115. doi:[10.1029/2009je003411](https://doi.org/10.1029/2009je003411).

625 Holstein-Rathlou C, Merrison J, Iversen JJ, Jakobsen AB, Nicolajsen R, Nørnberg P, Rasmussen K, Merlone
626 A, Lopardo G, Hudson T, Banfield D, Portyankina G. An environmental wind tunnel facility for testing meteorological sensor systems. *Journal of Atmospheric and Oceanic Technology* 2014;31(2):447–57. doi:[10.1175/jtech-d-13-00141.1](https://doi.org/10.1175/jtech-d-13-00141.1).

629 Jeong J, Hussain F. On the identification of a vortex. *Journal of Fluid Mechanics* 1995;285:69. doi:[10.1017/s0022112095000462](https://doi.org/10.1017/s0022112095000462).

631 Kolmogorov AN. The local structure of turbulence in incompressible viscous fluid for very large reynolds
632 numbers. *Proceedings: Mathematical and Physical Sciences* 1991;434(1890):9–13.

633 Lorenz RD, Merrison J, Iversen JJ. Wind Noise and Sound Propagation Experiments in the Aarhus Mars Atmosphere Simulation Chamber. In: *The Sixth International Workshop on the Mars Atmosphere: Modelling and Observation*. Granada, Spain; 2017. .

636 Martínez GM, Newman CN, Vicente-Retortillo AD, Fischer E, Renno NO, Richardson MI, Fairén AG, Genzer
637 M, Guzewich SD, Haberle RM, Harri AM, Kempainen O, Lemmon MT, Smith MD, de la Torre-Juárez
638 M, Vasavada AR. The modern near-surface martian climate: A review of in-situ meteorological data from
639 viking to curiosity. *Space Science Reviews* 2017;212(1-2):295–338. doi:[10.1007/s11214-017-0360-x](https://doi.org/10.1007/s11214-017-0360-x).

640 Martire L, Garcia RF, Rolland LM, Spiga A, Lognonné PH, Banfield DJ, Banerdt WB, Martin R. Martian
641 Infrasound: Numerical Modeling and Analysis of InSight's Data. *Journal of Geophysical Research: Planets*

642 in press;doi:[10.1029/2020JE006376](https://doi.org/10.1029/2020JE006376).

643 McDonald JA, Herrin E. Properties of pressure fluctuations in an atmospheric boundary layer. *Boundary-Layer*
644 *Meteorology* 1975;8(3-4):419–36. doi:[10.1007/bf02153561](https://doi.org/10.1007/bf02153561).

645 Morgan S, Raspet R. Investigation of the mechanisms of low-frequency wind noise generation outdoors. *The*
646 *Journal of the Acoustical Society of America* 1992;92(2):1180–3. doi:[10.1121/1.404049](https://doi.org/10.1121/1.404049).

647 Murdoch N, Chide B, Lasue J, Cadu A, Sournac A, Bassas-Portús M, Jacob X, Merrison J, Iversen J, Moretto
648 C, Velasco C, Parès L, Hynes A, Godiver V, Lorenz R, Cais P, Bernadi P, Maurice S, Wiens R, Mimoun
649 D. Laser-induced breakdown spectroscopy acoustic testing of the mars 2020 microphone. *Planetary and*
650 *Space Science* 2019;165:260–71. doi:[10.1016/j.pss.2018.09.009](https://doi.org/10.1016/j.pss.2018.09.009).

651 Murdoch N, Mimoun D, Garcia RF, Rapin W, Kawamura T, Lognonné P, Banfield D, Banerdt WB. Evaluating
652 the wind-induced mechanical noise on the InSight seismometers. *Space Science Reviews* 2016;211(1-
653 4):429–55. doi:[10.1007/s11214-016-0311-y](https://doi.org/10.1007/s11214-016-0311-y).

654 Murdoch N, Spiga A, Lorenz R, Garcia R, Perrin C, Widmer-Schnidrig R, Rodriguez S, Compaire N, Warner
655 NH, Mimoun D, Banfield D, Lognonné P, Banerdt W. Constraining Martian regolith parameters and vortex
656 trajectories from combined seismic and meteorological measurements. *Journal of Geophysical Research:*
657 *Planets* submitted;.

658 Neise W, Michel U. *Aerodynamic noise of turbomachines*. 1994. doi:[10.13140/2.1.3408.9760](https://doi.org/10.13140/2.1.3408.9760).

659 Norton MP, Karczub DG. *Fundamentals of Noise and Vibration Analysis for Engineers*. Cambridge University
660 Press, 2003. doi:[10.1017/cbo9781139163927](https://doi.org/10.1017/cbo9781139163927).

661 Read PL, Galperin B, Larsen SE, Lewis SR, Määttänen A, Petrosyan A, Rennó N, Savijärvi H, Siili T, Spiga
662 A, Toigo A, Vázquez L. The martian planetary boundary layer. In: Haberle RM, Clancy RT, Forget F,
663 Smith MD, Zurek RW, editors. *The Atmosphere and Climate of Mars*. Cambridge University Press; 2016.
664 p. 172–202. doi:[10.1017/9781139060172.007](https://doi.org/10.1017/9781139060172.007).

665 Schofield JT, Barnes JR, Crisp D, Haberle RM, Larsen S, Magalhães JA, Murphy JR, Seiff A, Wilson G.
666 The mars pathfinder atmospheric structure investigation/meteorology (ASI/MET) experiment. *Science*
667 1997;278(5344):1752–8. doi:[10.1126/science.278.5344.1752](https://doi.org/10.1126/science.278.5344.1752).

668 Smith MD, Wolff MJ, Lemmon MT, Spanovich N, Banfield D, Budney CJ, Clancy RT, Ghosh A, Landis
669 GA, Smith P, Whitney B, Christensen PR, Squyres SW. First atmospheric science results from the mars
670 exploration rovers mini-TES. *Science* 2004;306(5702):1750–3. doi:[10.1126/science.1104257](https://doi.org/10.1126/science.1104257).

671 Spiga A. Elements of comparison between martian and terrestrial mesoscale meteorological phenomena:
672 Katabatic winds and boundary layer convection. *Planetary and Space Science* 2011;59(10):915–22. doi:[10.](https://doi.org/10.1016/j.pss.2010.04.025)
673 [1016/j.pss.2010.04.025](https://doi.org/10.1016/j.pss.2010.04.025).

674 Spiga A, Banfield D, Teanby NA, Forget F, Lucas A, Kenda B, Manfredi JAR, Widmer-Schnidrig R, Murdoch
675 N, Lemmon MT, Garcia RF, Martire L, Özgür Karatekin, Maistre SL, Hove BV, Dehant V, Lognonné P,
676 Mueller N, Lorenz R, Mimoun D, Rodriguez S, Beucler É, Daubar I, Golombek MP, Bertrand T, Nishikawa

677 Y, Millour E, Rolland L, Brissaud Q, Kawamura T, Mocquet A, Martin R, Clinton J, Stutzmann É, Spohn
678 T, Smrekar S, Banerdt WB. Atmospheric science with InSight. *Space Science Reviews* 2018;214(7).
679 doi:[10.1007/s11214-018-0543-0](https://doi.org/10.1007/s11214-018-0543-0).

680 Spiga A, Forget F, Lewis SR, Hinson DP. Structure and dynamics of the convective boundary layer on mars
681 as inferred from large-eddy simulations and remote-sensing measurements. *Quarterly Journal of the Royal*
682 *Meteorological Society* 2010;;414–28doi:[10.1002/qj.563](https://doi.org/10.1002/qj.563).

683 Strasberg M. Dimensional analysis of windscreen noise. *The Journal of the Acoustical Society of America*
684 1988;83(2):544–8. doi:[10.1121/1.396148](https://doi.org/10.1121/1.396148).

685 Viúdez-Moreiras D, Gómez-Elvira J, Newman C, Navarro S, Marin M, Torres J, de la Torre-Juárez M. Gale
686 surface wind characterization based on the mars science laboratory REMS dataset. part i: Wind retrieval
687 and gale's wind speeds and directions. *Icarus* 2019;319:909–25. doi:[10.1016/j.icarus.2018.10.011](https://doi.org/10.1016/j.icarus.2018.10.011).

688 Walker KT, Hedlin MA. A review of wind-noise reduction methodologies. In: *Infrasound Monitoring for*
689 *Atmospheric Studies*. Springer Netherlands; 2009. p. 141–82. doi:[10.1007/978-1-4020-9508-5_5](https://doi.org/10.1007/978-1-4020-9508-5_5).

690 Wiens RC, Maurice S, Perez FR. The supercam remote sensing instrument suite for the mars 2020
691 rover mission: A preview. *Spectroscopy* 2017;32(5):50–5. URL: [http://www.spectroscopyonline.com/
692 supercam-remote-sensing-instrument-suite-mars-2020-rover-preview](http://www.spectroscopyonline.com/supercam-remote-sensing-instrument-suite-mars-2020-rover-preview).

693 Zakis JA. Wind noise at microphones within and across hearing aids at wind speeds below and above
694 microphone saturation. *The Journal of the Acoustical Society of America* 2011;129(6):3897–907. doi:[10.
695 1121/1.3578453](https://doi.org/10.1121/1.3578453).